Constraining Martian Regolith and Vortex Parameters From Combined Seismic and Meteorological Measurements

Naomi Murdoch, A. Spiga, R. Lorenz, Raphaël F. Garcia, C. Perrin, R. Widmer-schnidrig, S. Rodriguez, Nicolas Compaire, N. H. Warner, David Mimoun, et al.

JGR Planets

RESEARCH ARTICLE
10.1029/2020JE006410

Special Section:
InSight at Mars

Constraining Martian Regolith and Vortex Parameters From Combined Seismic and Meteorological Measurements

N. Murdoch[1], A. Spiga[2,3], R. Lorenz[4], R. F. Garcia[1], C. Perrin[5], R. Widmer-Schnidrig[6], S. Rodriguez[5], N. Compaire[1], N. H. Warner[7], D. Mimoun[1], D. Banfield[8], P. Lognonné[5], and W. B. Banerdt[9]

[1]Institut Supérieur de l'Aéronautique et de l'Espace (ISAE-SUPAERO), Université de Toulouse, Toulouse, France, [2]Laboratoire de Météorologie Dynamique/Institut Pierre Simon Laplace (LMD/IPSL), Sorbonne Université, Centre National de la Recherche Scientifique (CNRS), École Polytechnique, École Normale Supérieure (ENS), Campus Pierre et Marie Curie BC99, Paris, France, [3]Institut Universitaire de France, Paris, France, [4]Johns Hopkins Applied Physics Laboratory, Laurel, MD, USA, [5]Institut de physique du globe, CNRS, Université de Paris, Paris, France, [6]Black Forest Observatory, Stuttgart University, Wolfach, Germany, [7]Department of Geological Sciences, SUNY Geneseo, Geneseo, NY, USA, [8]Cornell Center for Astrophysics and Planetary Science, Cornell University, Ithaca, NY, USA, [9]Jet Propulsion Laboratory, California Institute of Technology, Pasadena, CA, USA

Key Points:

- Elastic properties of the Martian subsurface can be constrained using simultaneous pressure and seismic measurements of convective vortices
- Our modeling can also be used to constrain Martian convective vortex properties and to reconstruct the vortex trajectories
- The results indicate that the Martian ground may be harder to the west of InSight, consistent with geomorphological surface interpretations

Correspondence to:
N. Murdoch,
naomi.murdoch@isae.fr

Citation:
Murdoch, N., Spiga, A., Lorenz, R., Garcia, R. F., Perrin, C., Widmer-Schnidrig, R., et al. (2021). Constraining Martian regolith and vortex parameters from combined seismic and meteorological measurements. *Journal of Geophysical Research: Planets*, *126*, e2020JE006410. https://doi.org/10.1029/2020JE006410

Received 6 FEB 2020
Accepted 21 JAN 2021

Abstract The InSight mission landed on Mars in November 2018 and has since observed multiple convective vortices with both the high performance barometer and the low-noise seismometer SEIS that has unprecedented sensitivity. Here, we present a new method that uses the simultaneous pressure and seismic measurements of convective vortices to place constraints on the elastic properties of the Martian subsurface and the Martian vortex properties, while also allowing a reconstruction of the convective vortex trajectories. From data filtered in the (0.02–0.3 Hz) frequency band, we estimate that the mean value of η ($\eta = E/[1-\nu^2]$, where E is the Young's modulus and ν is the Poisson's ratio) of the Martian ground in the region around SEIS is 239 ± 140 MPa. In addition, we suggest that the previously reported paucity of vortex seismic observations to the west of InSight may be due to the fact that the ground is harder to the west than to the east, consistent with geomorphological surface interpretations.

Plain Language Summary In 2018, the InSight mission placed a seismic instrument on the surface of Mars in order to measure the motion of the Martian ground. As on Earth, there are fluctuations of pressure in the Martian atmosphere caused by small local variations in the atmospheric weight. Whirlwinds, for example, have a lower pressure in their center and they pull up the ground (like a vacuum cleaner). Such changes in pressure deform the elastic Martian ground and the InSight seismic instrument is sensitive enough to measure these deformations. We present a new method that uses the InSight pressure and seismic measurements of whirlwinds in order to determine how hard or soft the Martian ground is. We are also able to estimate the path that the whirlwinds follow as they pass by InSight. We find that the surface material just under InSight has elastic properties similar to dense gravel, but that the whirlwinds detected by the seismic instrument are not in the same places as the whirlwinds tracks observed from space. Our results suggest that the ground is harder to the west and, consequently, that it is more difficult for whirlwinds to deform the ground and create a seismic signal in that region.

1. Introduction

The InSight mission (Interior Exploration using Seismic Investigations, Geodesy, and Heat Transport mission; Banerdt et al., 2020) landed on Mars in November 2018 within a quasicircular depression called Homestead hollow (Figure 1; Golombek et al., 2020) in the Elysium Planitia region. Since then, the InSight mission has been performing the first comprehensive surface-based geophysical investigation of Mars using the SEIS (Seismic Experiment for Interior Structure; Lognonné et al., 2019) instrument. This low-noise seismometer with unprecedented sensitivity (Lognonné et al., 2020) contains three long period or very broad band (VBB) sensors and three short period (SP) sensors (Lognonné et al., 2019). To support the seismic measurements InSight also has a high performance barometer, and temperature and wind sensors

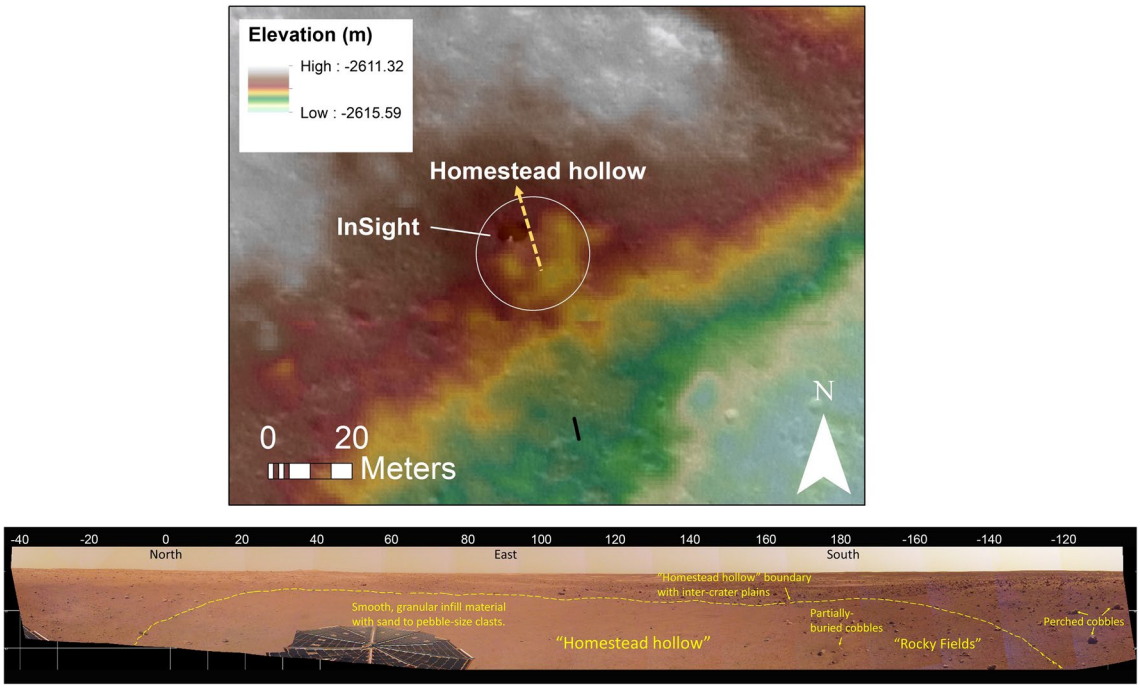

Figure 1. Top: High Resolution Imaging Science Experiment (HiRISE) digital elevation model at 1 m grid spacing overlain on a HiRISE image at 25 cm/pixel. The boundary of Homestead hollow is shown. The lander rests on the northwest interior margin of the hollow. The yellow arrow indicates the approximate straight-line trajectory calculated from the SEIS tilt azimuth at closest approach for the event on sol 133 (April 12, 2019) at 9:51 UTC (12:34 LMST). The SEIS tilt azimuth at closest approach for this event is 72° (Figure 9), close to the median SEIS tilt azimuth of all of the vortex events studied in the paper (69°; Figure 11) thus the arrow also represents the most common trajectory for the vortices studied here. Bottom: Instrument Deployment Camera partial panorama looking south, west, and north across the interior of Homestead hollow. Note the transition from smooth, infill materials to rockier terrain beyond the extent of the hollow.

(Temperature and Winds for InSight—TWINS) as part of its meteorological package (Banfield et al., 2019, 2020; Spiga et al., 2018).

During the mission preparation extensive efforts were made to understand the different noise contributions that were likely to be observable by the SEIS instrument once deployed onto the surface of Mars (Mimoun et al., 2017), with a particular focus placed on understanding the atmosphere-generated seismic signals (Kenda et al., 2017; Murdoch et al., 2017a, 2017b; Spiga et al., 2018). One such seismic signal, that has been long-identified and studied on Earth, is the elastic deformation of the ground due to fluctuations of atmospheric pressure (Sorrells, 1971; Sorrells et al., 1971). The pressure fluctuations induce a ground tilt that is observed by a seismometer placed on the surface. On Earth, this effect can be minimized by placing seismometers in deep underground vaults. However, SEIS is deployed directly onto the Martian surface, covered with a Wind and Thermal Shield (WTS; Figure 2).

One specific type of atmospheric pressure variation that has been predicted to generate seismic signals observable by SEIS is convective vortices (Murphy et al., 2016), also known as dust devils when the vortex transports dust particles. A convective vortex forms when warm air close to the surface starts to rise and begins to rotate, generating a pressure depression in the center (Rafkin et al., 2016). This depression creates a suction effect, pulling the elastic ground upwards and tilting the surface away from the vortex. Convective vortices are detectable in pressure measurements as a sharp drop in the pressure time series lasting typically 10–100 s (Murphy et al., 2016). The first seismic detection of a terrestrial convective vortex was in 2015 (Lorenz et al., 2015), and the InSight seismometers (and barometer) have since detected multiple convective vortices on the surface of Mars (Banerdt et al., 2020; Banfield et al., 2020; Lognonné et al., 2020).

The simplest model of a convective vortex encounter is the straight-line, constant-speed migration of a negative point load on an elastic half-space. As the vortex migrates, the ground is deformed by the negative point load and the resulting ground displacement at the seismometer can be simulated as a function of time.

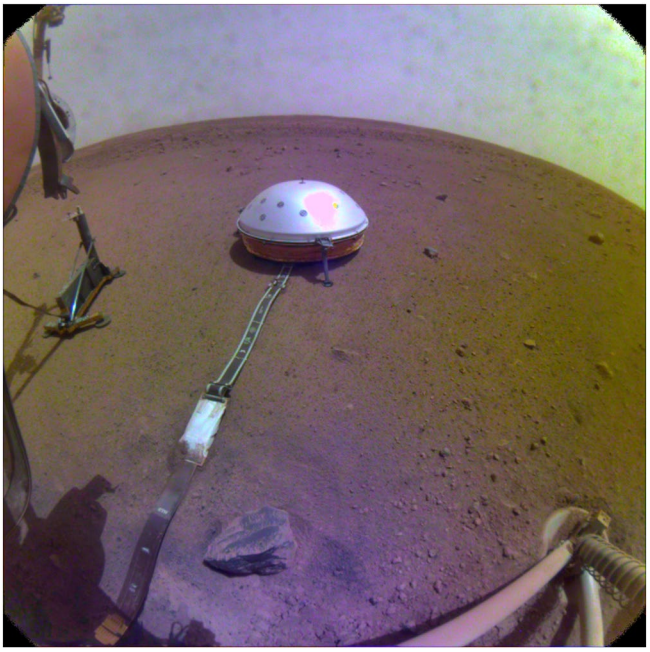

Figure 2. SEIS and the "Wind and Thermal Shield" deployed on the surface of Mars. This image, taken by InSight's context camera, also shows the electrical cable linking SEIS to the lander, the Heat Flow, and Physical Properties Package instrument to the left of SEIS, and one of the lander feet in the bottom right of the image. Image courtesy of NASA/JPL/Justin Maki.

Prior to the InSight landing, such a point-source model was developed and validated by fitting both seismic and pressure observations of terrestrial dust devils (Lorenz et al., 2015).

The point-source approach assumes that the strain applied to the ground is very small (i.e., there is no plastic deformation), and that the convective vortex passes at a distance of at least one vortex diameter from the seismometer (for closer approaches, the spatial extent of the vortex must be taken into account and a finite element method should be used, for example, Murdoch et al., 2017b). The point-source modeling approach is extremely useful in order to describe the full time series of the convective vortex signal. However, finding suitable parameter solutions requires time-consuming Monte Carlo simulations.

Prior to their seismic detections, observations of Martian vortices have been based on four methods (for a review, see Murphy et al., 2016): Imaging from orbit, imaging from surface, surface pressure measurements, and surface wind measurements. Imaging-based observations provide trajectory information, however they do not provide physical measurements on the strengths of the vortices (i.e., central pressure drops). Long time series of pressure measurements can be used to provide information on the strength distribution, however not on trajectories (Kurgansky, 2019). Wind measurements give information about vortex direction of motion and rotation direction (clockwise or counterclockwise), however miss distances can only be determined from wind measurements if the encounter is very close, and even then with large error margins (Kahanpää & Viúdez-Moreiras, 2020; Ringrose et al., 2003; Tratt et al., 2003).

In the context of the InSight mission, modeling the effect of vortices on the seismic and pressure data has contributed to providing the first constraints on the average properties of the shallow elastic structure of Mars (Lognonné et al., 2020). These initial analyses used the plane wave approach of Sorrells' theory (Kenda et al., 2020). The point-source modeling approach has also been used to interpret joint observations of a dust devil vortex by orbital imaging (High Resolution Imaging Science Experiment; HiRISE), in situ imaging, SEIS, and the InSight pressure and wind sensors (Banerdt et al., 2020). Through waveform fitting, the simple vortex model allowed the dust devil pressure drop event to be identified among the numerous pressure drops present in the data. Combining the information from the multiple instruments then allowed detailed calculations to be made of the compliance of the Martian subsurface in a specific known location (Banerdt et al., 2020).

Here, we propose a computationally inexpensive method to place constraints on the vortex parameters (strength, size, and miss distance), and the elastic properties of the Martian subsurface using simultaneous pressure and seismic measurements of convective vortices. We also demonstrate how our modeling can be used to reconstruct the convective vortex trajectories. The method developed here allows quantitative estimates to be made of the Martian subsurface properties around the InSight lander. Based on our results, we discuss the geological implications of the InSight vortex observations, specifically with respect to the paucity of SEIS measurements of vortices to the west of InSight.

2. Meteorological and Seismic Observations of Convective Vortices on Mars With InSight

2.1. Meteorological and Seismic Data

The InSight barometer and SEIS sensors acquire data continuously at 20 samples per second (sps) and 100 sps, respectively. This data is downsampled and the data transmitted to Earth typically has sampling rates of 2 sps for the barometer and 10 sps for the VBB data up until Sol 175, and then 10 and 20 sps for the barometer and VBB data, respectively, for subsequent sols (a sol is a Martian day, with InSight Sol 0 being the day InSight landed on Mars). In this paper, we use the continuous high gain science mode VBB velocity (VEL)

data (Lognonné et al., 2019). The TWINS wind data are acquired using two sensors, typically at acquisition rates of 0.1 or 1 sps (Spiga et al., 2018). The data are then calibrated and combined to provide measurements of the horizontal wind speed and direction. Details about where the raw and calibrated data can be obtained are provided in the Acknowledgments at the end of this paper.

The seismic data preprocessing we perform involves removing the instrument response and rotating the three VBB components U, V, and W into Z, N, E (Z being positive upwards). To remove any potential artifacts induced by the sampling rate, we also downsample the high sampling rate data (seismic and pressure) using the same algorithms as the InSight flight software (Lognonné et al., 2019). We then filter the data (in the [0.02–0.3 Hz] frequency band for this study), before converting the velocity data to acceleration and extracting the time window around the specific vortex we want to study. For investigations using both seismic and pressure data, the pressure data are always filtered in the same bandwidth as the seismic data.

To interpret the output of SEIS in terms of ground tilt we have to establish the sign conventions for acceleration and for tilt. SEIS operates based on the principle of an inertial accelerometer where accelerations are measured by sensing the distance between the frame and a proof mass suspended on a spring (Lognonné et al., 2019). For SEIS, positive output signals on the Z, N, and E channels denote positive accelerations of the instrument frame in the vertical-up, north, and east directions, respectively. Furthermore, we adopt the usual convention for the tilt angle θ: it is measured away from the horizontal and increasing in the downward direction. In its level position the sensitive directions of the two horizontal components are perpendicular to the gravity acceleration, g. However, as soon as the seismometer frame gets tilted by a small angle θ the proof mass experiences the projection of the acceleration of gravity $g * \sin(\theta) \simeq g\theta$: for a downward tilt in the east direction gravity will pull the proof mass in the east direction and hence the output of the seismometer indicates an acceleration of its frame in the west direction. Thus, when we interpret an acceleration signal in terms of ground tilt a positive acceleration points in the uphill direction or equivalently in the direction of negative tilt. A value of $g = 3.71$ m/s^2 is assumed for the Martian gravity acceleration in this study.

2.2. Vortex Identification

The convective vortices are identified in the pressure data (sols 75–200) as instances where the drop in pressure is at least 0.3 Pa with respect to a smoothed 1,000-s window (the convective vortex identification method is described in detail in Spiga et al., 2020). Once identified in the pressure data, they can also be identified in the seismic data. As described in the following section, in this paper, we focus on pressure drops that have a nice "clean" pressure drop, determined by the goodness of fit to a Lorentzian profile (the goodness of fit must be > 0.5). This allows us to eliminate pressure drops linked to convective cells in the atmosphere rather than vortices, to avoid more complex pressure drops involving, for example, multiple vortices. Additionally, we reduce the probability of including "glitches"; a frequent artifact in the VBB data (Scholz et al., 2020).

The goodness of fit between the analytical pressure model p and the pressure data p_{data} is defined as follows:

$$fit = 1 - \| p - p_{\text{data}} \| / \| p - mean(p_{\text{data}}) \| \quad (1)$$

where $\|$ indicates the 2-norm of a vector and fit values can vary between -∞ (bad fit) and 1 (perfect fit).

2.3. Vortex Profile

A key question is the analytical profile of pressure with respect to radius within convective vortices, that is, how the vortex pressure deficit magnitude declines with increasing distance from the center of the depression.

Several models have been proposed previously to describe the pressure field (ΔP) of convective vortices as a function of the distance from the center of the vortex (r), the diameter of the vortex (D, defined as the half-maximum diameter of the pressure depression of the vortex), and the vortex central pressure deficit (ΔP_o). The three major analytical functions are provided in Equations 2–4, from Vatistas et al. (1991), Ellehoj et al. (2010), and Lorenz et al. (2015), respectively.

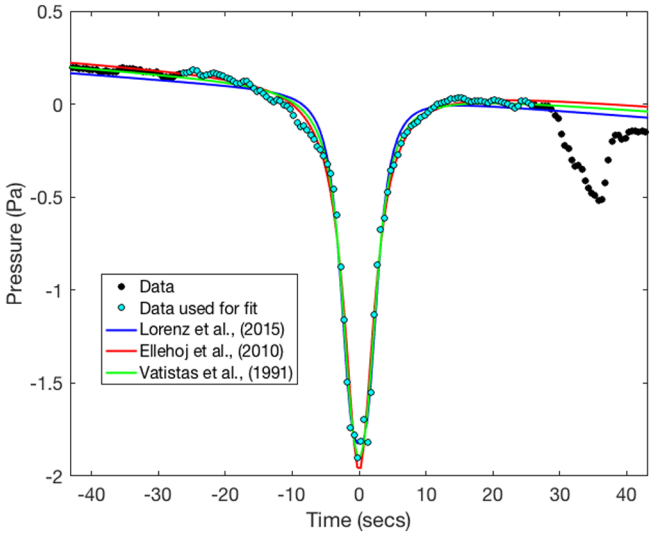

Figure 3. A vortex-induced pressure drop detected on Sol 133 (April 12, 2019) at 9:51 UTC (12:34 LMST) is shown here by the black markers, on a diagram having the time axis in seconds centered on the pressure drop. The part of the pressure drop considered for the analysis is colored in cyan. Comparisons with analytical shapes are added in the figure: Lorenz et al. (2015) (blue line), Vatistas et al. (1991) (green line), and Ellehoj et al. (2010) (red line). The pressure data has been detrended by removing frequencies below 1 mHz.

$$\Delta P(r) = \Delta P_o(1 / [1 - (2 / \pi)\arctan(2r / D)^2 + 1]) \quad (2)$$

$$\Delta P(r) = \Delta P_o(1 / [(2r / D)^2 + 1]) \quad (3)$$

$$\Delta P(r) = \Delta P_o(1 / [(2r / D)^3 + 1]) \quad (4)$$

Currently there is no clear consensus on which expression should be used as the different models all have relatively good fits to the Martian dust devil population (e.g., Balme & Greeley, 2006). Here, we use the pressure time series during vortex events to investigate which model is the most appropriate for vortices measured by the InSight pressure sensor—more sophisticated approaches combining pressure and wind measurements, such as the one envisioned in Jackson et al. (2018) are left for future studies.

Our practical methodology is as follows: we detrended the pressure data by removing frequencies below 1 mHz. Then we extract a time series in a window of 200 s centered on the pressure drop. To indicate the pressure drops being smooth enough for our analysis, and to evaluate the usability of the three functions provided above, the data of all events are fitted to each of the functions. In this simple approach, the diameter D of the vortex is assumed to be equivalent to $S\tau$, τ being the full width half-maximum (FWHM) of the pressure depression in the time series and S the vortex advection speed. As the distance x is equivalent to St, the vortex translational speed drops out of the above equations and the time (t, τ) and distance (r, D) parameters can be used interchangeably in the analysis framework we chose here.

We use a normalized root mean square error cost function in order to determine the goodness of fit of the pressure data to the analytical functions. When considering only the vortex events which provide a goodness of fit of at least 0.5 for all three models (which sums up to 633 events from sols 75–200 of InSight considered for this particular analysis), we obtain a mean goodness of fit of about 0.7 for all models. An example of fitting a representative individual event is shown in Figure 3. There is no particular evolution of the goodness of fit with sol number; and when considering the mean wind speed and direction during the duration of each vortex event, the selected good-fit events are representative of the full distribution.

However, despite these analysis suggesting that no particular model can be deemed more suitable than another, there are indications from recent combined seismic and pressure analyses with InSight data that the "Ellehoj" or "Vatistas" pressure models may be more appropriate (Banerdt et al., 2020). Specifically, for a dust devil passing at known distance from InSight, the parameter space retrieved for the vortex properties is more reasonable for these models than for the r^3 pressure model (Equation 4). In addition, multiple observations (Kenda et al., 2020; Lognonné et al., 2020) have indicated that for a homogeneous ground, the derived compliance should be invariant with the distance. Adopting either the "Ellehoj" or "Vatistas" pressure models also ensures that this criterion is upheld as the ratio of the observed pressure deficit and the ground tilt is independent of the distance (as shown in Banerdt et al., 2020).

Given these considerations, and that the "Ellehoj model" (Lorentzian function) has been successfully used in several studies of Martian dust devils (e.g., Ellehoj et al., 2010; Kahanpää et al., 2016; Newman et al., 2019), we adopt this model (Equation 3) for the present study.

For the rest of this study, for each vortex, the maximum pressure deficit of the vortex pressure profile measured during the vortex encounter (ΔP_{obs}), and the FWHM of the pressure profile in the time series (τ) are found using the "Ellehoj" function fit to the (filtered) pressure data. It should, however, be noted that Lorenz et al. (2021) show that many vortex pressure traces measured by InSight are skewed (the attack

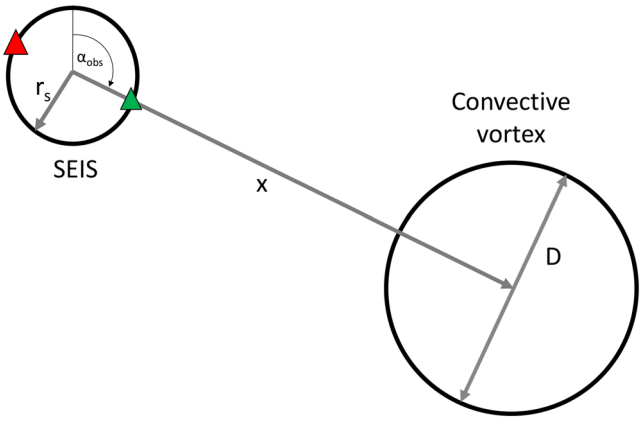

Figure 4. The encounter geometry showing the miss distance, x, between the center of SEIS and the center of the vortex. The tilt azimuth is shown by α_{obs}, which also indicates the azimuth of the center of the vortex. r_s is the radial distance from the geometric center of the seismometer to the circle upon which the three seismometer feet lie, and D is the diameter of the vortex. The radial tilt, in the direction of the vortex, is calculated from the difference in vertical displacement between the points indicated by the red and green triangles (see Equation 13).

time is longer than the decay time) implying that the surface pressure field around a vortex being advected in the wind is not strictly circularly symmetric, as we assume in this paper.

2.4. Background Wind Speeds

The mean background wind speed v for each pressure drop is estimated using a 200 s window centered on the time of vortex closest approach. To remove influence of the vortex winds, we exclude the time window of $\pm$ 5τ around the vortex encounter. The 1σ_v value of the wind speed used below is the standard deviation of the wind speed measurements in the same time window.

2.5. Radial Tilt and Azimuth

θ_{obs} is defined as the maximum value of radial tilt (in radians) measured during the vortex encounter, that is,

$$\theta_{obs} = \max\left[\frac{\sqrt{(A_E^2 + A_N^2)}}{g}\right] \quad (5)$$

where A_E and A_N are the VBB acceleration measurements in the east and north directions, respectively.

The vortex azimuth, α, is the four-quadrant inverse tangent of A_E and A_N, defined in the interval (−180°, 180°) where 0° and 90° indicate North and East, respectively. These angles are indicated in the context images in Figure 1. The vortex azimuth at the closest approach (α_{obs}) is the value of α when the observed radial tilt is at its maximum (Figure 4).

We note that these analyses focus on the horizontal tilt component of the seismic signal and neglect the inertial component of the horizontal seismic signal. This is considered to be reasonable given that, for a homogenous half space approximation, the horizontal tilt component is expected to dominate the horizontal inertial component in the (0.02–0.3 Hz) frequency band used here (Kenda et al., 2020).

2.6. Typical Vortex Observation

An example observation by InSight of a "classical" convective vortex seismic signal, as first described in Lorenz et al. (2015), is given in Figure 5 centered around 100 s. At the same time as the vortex is detected as a drop in pressure in the barometer data, the horizontal (N, E) seismic axes clearly show the tilt signature, and the vertical (Z) seismic axis shows the ground acceleration due to the upward ground motion as the vortex passes by. For this particular example, the positive signal on the E component implies a ground tilt in the west direction and, from the "heartbeat"-shaped N component (80–120 s in Figure 5), we can determine that the ground tilted first toward the north and then toward the south. These measurements indicate, therefore, a vortex trajectory moving from the south to the north and passing to the east of SEIS (see Section 5.3 for more details).

3. Using Combined Seismic and Meteorological Observations to Determine Ground and Vortex Properties

Here, we propose a computationally inexpensive method to constrain the vortex and ground properties using purely analytical considerations. The point source model can then be used to reconstruct, and refine, the full vortex trajectory (Section 5.3).

It is assumed that the pressure depression of the vortex ΔP depends only on the radial distance from the vortex center r. Hence, ΔP can be represented with the function

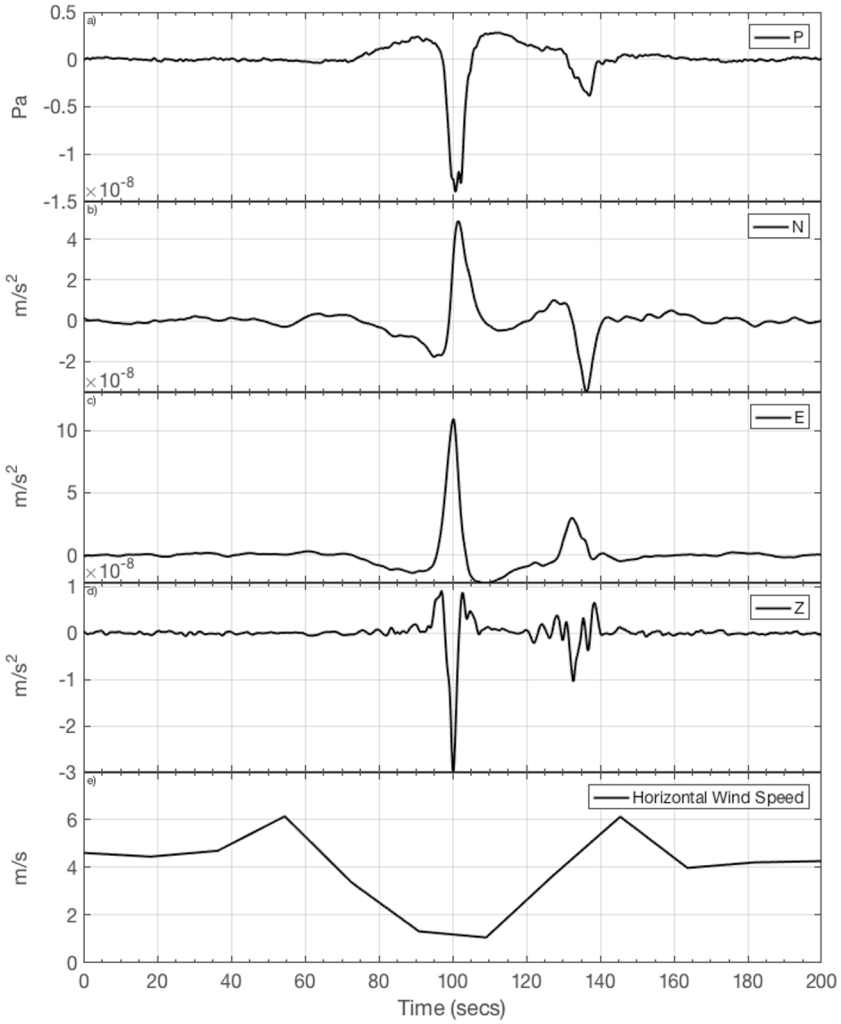

Figure 5. The pressure variation (P) measured by the barometer, the acceleration measured by the VBB sensor (N, E, and Z), and the horizontal wind speed measured by TWINS during 200 s around a convective vortex encounter. This event occurred on Sol 133 (April 12, 2019) at 9:51 UTC (12:34 LMST). In addition to the data processing described in Section 2, the data have been filtered in the (0.02–0.3 Hz) frequency band.

$$\Delta P = -\Delta P_o f(2r \,/\, D) \tag{6}$$

where the function f obtains the value 1 when its argument is 0 and the value 0 when the argument nears infinity, ΔP_o is the central pressure depression of the vortex, and D is a parameter defining its diameter. The (negative) load, F_z, of a convective vortex is the area integral of ΔP:

$$F_z(r) = -2\pi \int_0^\infty \Delta P_o f(2r \,/\, D) r dr. \tag{7}$$

By writing $2r/D = r_n \Leftrightarrow r = (D/2)r_n$ we obtain

$$F_z(r) = -2\pi \Delta P_o f(D \,/\, 2)^2 \int_0^\infty f(r_n) r_n dr_n, \tag{8}$$

which can be represented as

$$F_z = -\beta \Delta P_o D^2 \pi \tag{9}$$

where

$$\beta = \frac{1}{2}\int_0^\infty f(r_n) r_n dr_n. \tag{10}$$

β, therefore, depends on the peripheral pressure dependence of the vortex (example values of β for different pressure distributions are given in Section 4).

Following Section 2.3, we assume that the observed pressure deficit in a convective vortex can be modeled by the Lorentzian function given in Equation 4 (Ellehoj et al., 2010). Outside of the vortex core ($r \gg D/2$), this simplifies to:

$$\Delta P(r) = \Delta P_o D^2 \,/\, (4r^2) \tag{11}$$

The vertical deformation of the ground (d_z), at a distance r from a point source of vertical load F_z is given by (Boussinesq, 1885; Landau & Lifshitz, 1970):

$$d_z = F_z(1-\nu^2) \,/\, (\pi E r), \tag{12}$$

with E being the Young's modulus, and ν is Poisson's ratio of the elastic ground.

The ground tilt in radians (θ) along the axis of the line joining the vortex and the seismometer can be expressed as:

$$\theta = (d_{zi} - d_{zj}) \,/\, (2r_s) \tag{13}$$

where r_s is the radial distance from the geometric center of the seismometer (defined as the center of a circle drawn through the three SEIS feet) to the seismometer feet, d_{zi} is the ground displacement at a distance $r - r_s$ (green triangle in Figure 3) and d_{zj} is the ground displacement at a distance $r + r_s$ (red triangle in Figure 3). Using Equation 12, Equation 13 can then be expressed as:

$$\theta = [(F_z(1-\nu^2)) \,/\, (2r_s \pi E)][1 \,/\, (r - r_s) - 1 \,/\, (r + r_s)] \tag{14}$$

Far from the seismometer ($r \gg r_s$) this simplifies to:

$$\theta = F_z(1-\nu^2) \,/\, (\pi E r^2) \tag{15}$$

In the case of distant encounters ($r \gg D/2$), we can then write:

$$\theta_{\text{obs}} = \beta\zeta \,/\, (\eta r^2); \tag{16}$$

$$\Delta P_{\text{obs}} = \zeta \,/\, (4r^2). \tag{17}$$

where we define η and ζ to describe the ground parameters and the vortex parameters as follows:

$$\eta = E \,/\, (1-\nu^2); \tag{18}$$

$$\zeta = \Delta P_o D^2. \tag{19}$$

There are only a range of vortex and ground parameters that will provide simultaneous solutions to both the observed pressure and tilt data (ΔP_{obs} and θ_{obs}). However, the problem is degenerate; many combinations of the ground parameters (Poisson's ratio and Youngs' Modulus) and vortex parameters (core pressure drop, diameter, and miss distance) can provide the same seismic amplitude. Indeed, with this methodology, it is only possible to constrain η and ζ to describe the ground parameters and the vortex parameters, respectively.

We note that both Equations 16 and 17 vary with $1/r^2$ leading to a constant value for $\theta_{\text{obs}}/\Delta P_{\text{obs}}$, independent of the distance r, as discussed in Section 2.3 and shown by Banerdt et al. (2020). These can then be combined to provide an expression for η:

$$\eta = (4\beta\Delta P_{\text{obs}}) \,/\, \theta_{\text{obs}}; \tag{20}$$

In order to quantify ζ we use the following relationship between the vortex translational speed (S), the FWHM of the pressure drop time series (τ) and the vortex strength and size from Jackson et al. (2018):

$$\Delta P_o D^2 = \Delta P_{\text{obs}} (S\tau)^2; \tag{21}$$

$$\zeta = \Delta P_{\text{obs}} (S\tau)^2; \tag{22}$$

As vortices tend to follow the ambient wind field relatively closely (Balme et al., 2012; Stanzel et al., 2008), we assume that S can be approximated by the background wind speed v measured by TWINS at the time of the vortex encounter. We note, however, that this may be a lower limit to the advection speed given that vortices may actually translate with boundary layer wind speeds, hence up to 2 times faster than surface winds (Reiss et al., 2014).

Finally, we note that it is also possible to calculate the minimum distance between the vortex and the sensors (x) from Equations 17 and 22, again when $r \gg D/2$:

$$x = S\tau \,/\, 2; \tag{23}$$

Alternatively, x can be evaluated using the maximum amplitudes of ΔP_{obs} and θ_{obs} in Equations 16 or 17, that is,

$$x = \sqrt{\frac{\beta\zeta}{\eta \max(\theta_{\text{obs}})}}; \tag{24}$$

$$x = \sqrt{\frac{\zeta}{4 \max(\Delta P_{\text{obs}})}}; \tag{25}$$

In the following section, we will demonstrate how β can be determined. We note also that the ratio of the miss distance x and the translation velocity S can also be solved from the time series of the ground tilt data and this will be included in future work.

4. Determining the Value of β

The prefactor β depends on the assumed peripheral pressure dependence of the vortex. Lorenz et al. (2015) find $\beta = 0.5$ assuming the vortex pressure profile given in Equation 4 integrated over 5 r_{norm} ($r_{\text{norm}} = 2r/D$). Note that Lorenz et al. (2015) actually chose this pressure model because it can be integrated analytically, unlike the Lorentzian model provided by Ellehoj et al. (2010). Without analytical solutions, β could be determined for other vortex pressure profiles by numerically integrating the pressure load out to a given radius. For example, $\beta = 0.8$ for the "Ellehoj" Lorentzian vortex model used in this paper (Equation 3) also integrated over 5 r_{norm} ($r_{\text{norm}} = 2r/D$). However, without additional information this radius would be chosen somewhat arbitrarily.

In order to determine β we need a vortex for which we have seismic data, pressure data, a known miss distance and an estimate of the ground properties. This is the case for the vortex on Sol 202 (June 22, 2019) at 7:59 UTC (13:10 LMST) studied in detail in Banerdt et al. (2020) and discussed briefly in Lorenz et al. (2021) (Table 2, entry for Event #00368). A dust devil track in the close vicinity of the InSight lander was identified in both in situ InSight Context Camera images and orbital HiRISE images. Modeling results of the waveforms expected in the seismic and pressure measurements for the dust devil track allowed the most likely vortex candidate to be selected. Then, the observed combined seismic and pressure measurements of the identified vortex were used to estimate the ground properties. Table 1 provides the full list of parameters for this vortex event.

Using Equation 20, we find a value of $\beta = 1$ for the data filtered in the (0.02–0.3 Hz) frequency band. This is also within the range of β predicted from Equation 16, assuming that $(v - 1\sigma_v) < S < (v - 1\sigma_v)$: 0.8–2.8.

Table 1
Vortex and Ground Parameters Derived for the Vortex on Sol 202 (22nd June 2019) at 7:59 UTC (13:10 LMST)

Parameter	Symbol	Value
Vortex miss distance[a]	X	19 ± 1 m
Young's modulus[a]	E	2.7e8 Pa
Poisson's ratio[a]	N	0.22
Background wind speed[b]	V	9.8 ± 1.1 m/s
Maximum observed pressure deficit[b]	ΔP_{obs}	0.52 Pa
FWHM of the pressure vortex[b]	T	3.3 s
Maximum radial tilt[b]	θ_{obs}	7.5e-9 rad
$\Delta P_{obs} D^2$ [b]	ζ	749 Pa m^2

[a]From Banerdt et al. (2020).
[b]Calculated here (see text). Seismic and pressure data are filtered in the (0.02–0.3 Hz) frequency band.

The possible range of miss distance, calculated using the same range for the advection speed, and the encounter duration (Equation 23) is 11–21 m; consistent with the image observations indicating a distance of 19 ± 1 m.

We note that this analysis also allows us to determine ζ for this particular vortex, information that was not derived in Banerdt et al. (2020). Using Equations 16 or 17 we find a value of 749 Pa m^2 for ζ, which is compatible with the range predicted from Equation 22 and assuming that $(v - 1\sigma_v) < S < (v - 1\sigma_v)$: 270–928 Pa m^2.

It should also be noted that the value of β will vary with the filtering applied to the seismic and pressure data, but this is to be expected and represents the prefactor required to accurately represent a finite disperse load by a point source at different seismic frequencies. Given that β depends on the peripheral pressure dependence of the vortex (Equation 10), and that the surface pressure field around a vortex being advected in the wind is not strictly circularly symmetric Lorenz et al. (2021), it is also possible that β varies from vortex to vortex. Nonetheless, the effect of this variation likely cancels out when taking averages over large numbers of observations. Thus, β can be assumed constant and equal to 1 for the purposes of this study.

5. Results

Our precise methodology for studying the vortex and ground parameters is the following: For each vortex event, we consider the point of closest approach, that is, the maximum amplitudes of θ_{obs} and ΔP_{obs}. First, we solve Equation 20 to find η, assuming $\beta = 1$. Then, we solve Equation 22 to find the possible range of ζ assuming $(v - 1\sigma_v) < S < (v - 1\sigma_v)$. We also determine a range of possible miss distances (x) following Equation 23 (or Equations 24 or 25; they give identical results).

To be included in the analyses, the pressure drop (after detrended by removing frequencies below 1 mHz, and after filtering in the [0.02–0.3] Hz frequency band) must have a good fit to the "Ellehoj" pressure vortex model (goodness of fit > 0.5), the magnitude of ΔP_{obs} (after filtering in the [0.02–0.3] Hz frequency band) must be >0.2 Pa (note that this is smaller than the vortex identification threshold described in Section 2.2 due to the filtering applied), wind speed and seismic data must be available for the event, and the derived value of η should be in the range 1e7–1e10 Pa. We note also that to ensure that we are fitting the same event in the pressure and seismic data, the maximum amplitude of the radial tilt should occur within 2 s of the maximum amplitude of the observed pressure. If this is not the case, the event is excluded from the analyses. Four hundred and ninety-two pressure drops identified in the pressure time series (Section 2.2) met all of these criteria and were included in the final analyses.

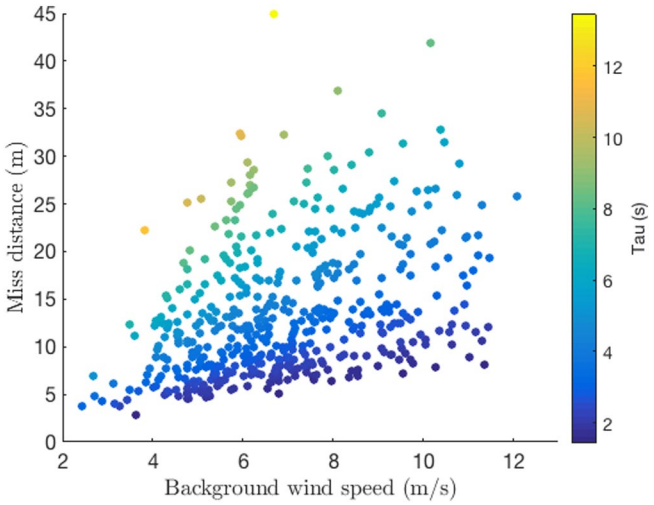

Figure 6. The miss distance (x) as a function of the vortex advection speed (S, assumed to be equal to the mean background wind speed v) for all vortex events considered in these analyses. The color represents the vortex encounter duration, τ.

5.1. Constraints on Vortex Properties at the InSight Landing Site

Assuming that $x \gg D$, the encounter duration depends only on the background wind speed and the miss distance with the largest encounter durations being for events with both large miss distances and low background wind speeds (Equation 23, Figure 6). Note that, for closer encounters, the vortex diameter also affects the encounter duration (Ellehoj et al., 2010; Kahanpää & Viúdez-Moreiras, 2020).

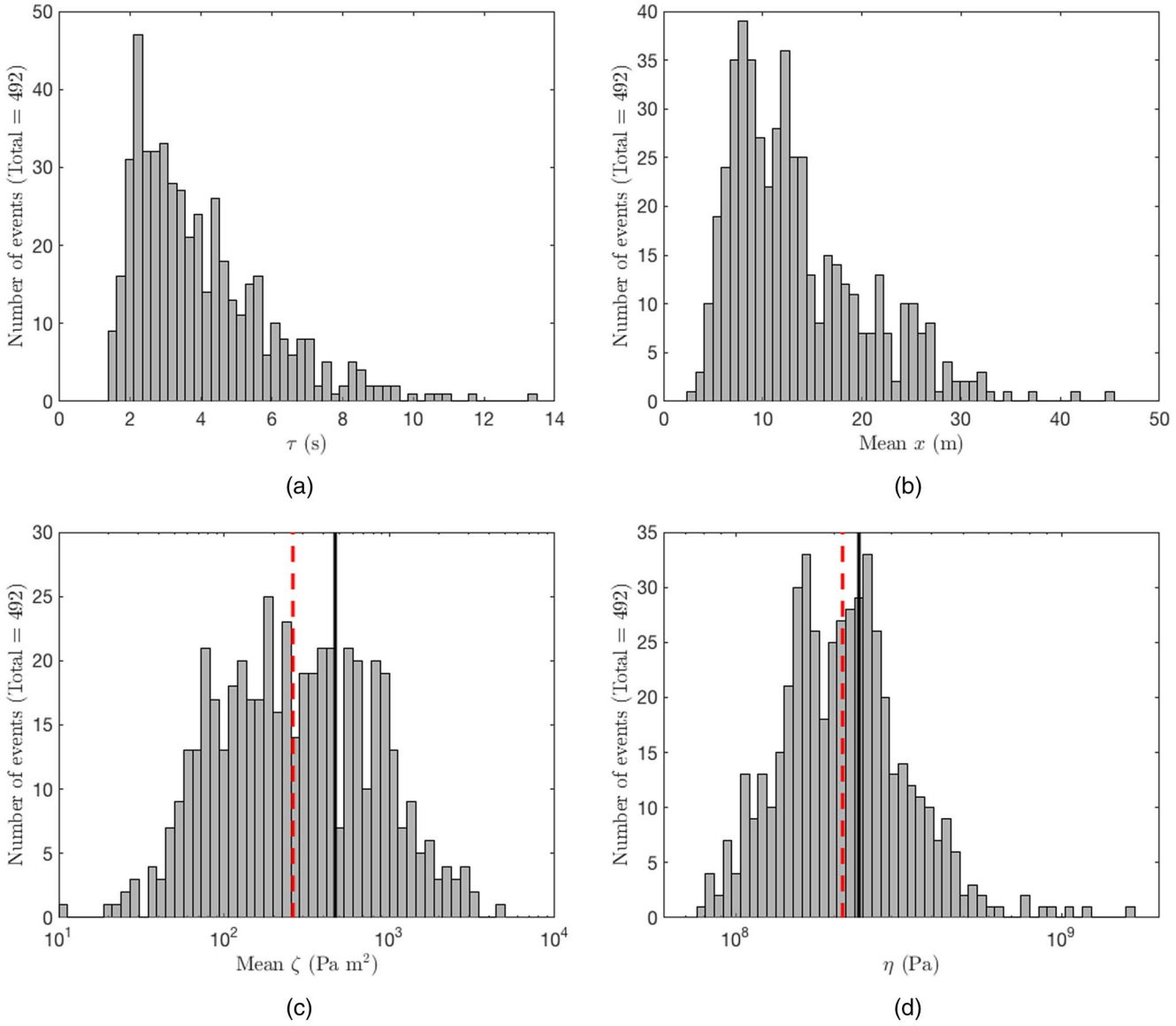

Figure 7. Histograms of (a) the encounter duration τ defined as the FWHM of the pressure deficit, (b) the mean miss distance x, (c) mean ζ where $\zeta = \Delta PD^2$, and (d) $\eta = E/(1-\nu^2)$ determined for 492 vortex events in the (0.02–0.3 Hz) frequency band between sols 75 and 200. Unique values of τ and η are determined for each vortex event, x and ζ depend on the advection speed S and the value reported is the value for the mean background wind in the 200 s window around the event, that is, when $S = v$. The mean and median values of ζ, shown by the solid black and red dashed lines in (c), are 470 and 261 Pa m^2, respectively. Similarly, the mean and median values of η, shown by the solid black and red dashed lines in (d), are 239 and 213 MPa, respectively.

As would be expected, the encounter duration is not observed to vary with the tilt azimuth at closest approach, nor with ground properties (η). A histogram of all of the encounter durations is provided in Figure 7a.

The encounter durations (FWHM) range from 1.4 to 13.5 s for the pressure data filtered in the [0.02–0.3 Hz] frequency band. A consequence of the filtering applied to the data for our particular analyses is that the longer period events are removed from the data set. The encounter durations are nonetheless similar to the encounter durations reported for the Phoenix Mars mission (mostly in the range of 5–15 s; Ellehoj et al., 2010), Mars Pathfinder (full durations of 15–51 s; Ferri et al., 2003), and MSL (1.4–20.3 s; Steakley & Murphy, 2016). Lorenz et al. (2021) present a catalog of 853 vortex events with $\Delta P_{obs} \geq 0.8$ Pa, detected by InSight over sols 0–390, which may be consulted for statistical properties of a wider set of InSight vortices, although many events discussed in the present paper are not included in that catalog since they have ΔP_{obs} less than this threshold.

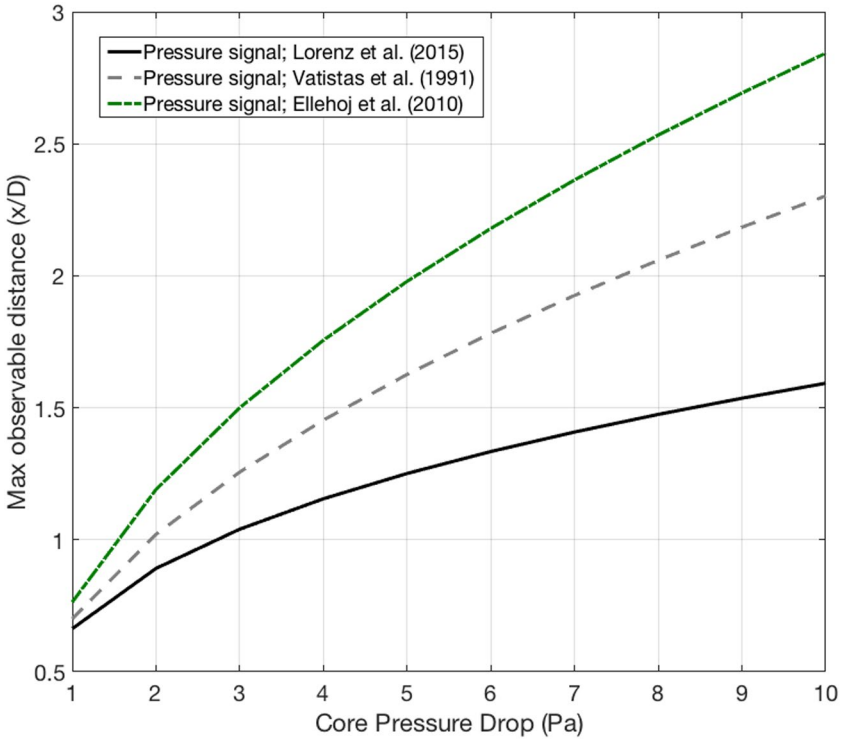

Figure 8. The normalized maximum observable distance of a convective vortex assuming a pressure drop detection threshold of −0.3 Pa. The green dashed line shows the results assuming a pressure distribution with distance from the vortex center as used above (Equation 3) and, for comparison, the solid black and dashed gray lines shows the results assuming alternative models (see Section 2.3).

A histogram of all of the miss distances is provided in Figure 7b, assuming that x ≫ D. The miss distances of the encounters studied here range from 3 to 45 m. As τ and x are proportionally related (Equation 23), the filtering we apply to the data that removes the longest period events also removes the events with the largest miss distances.

A histogram of all of the values of ζ obtained for all vortices analyzed in this study is provided in Figure 7c. The mean and median values are 470 and 261 Pa m^2, respectively. Similarly to the encounter duration, ζ is not observed to vary with the tilt azimuth at closest approach, nor with ground properties (η), as expected.

5.2. Constraints on the Elastic Properties of the Martian Ground at the InSight Landing Site

Figure 7d shows a histogram of η determined for the 492 vortex events between sols 75 and 200. The mean value for η, for all vortex events considered here, is found to be 239 ± 140 MPa, where the error is the standard deviation (the median value of η is 217 MPa).

As all of the vortices analyzed here were first identified in the pressure data, it is possible to estimate the size of the region around InSight that we are sampling by estimating the maximum observable distance of a vortex (Figure 8). For example, for a 3 Pa core pressure drop vortex of diameter 30 m, the detection distance for the pressure signal is in the range of 30–45 m, depending on the assumed pressure profile. Therefore, given the typical diameters (several meters to tens of meters), and core pressure drops (measured up to 9 Pa) of the Martian convective vortices (Banfield et al., 2020; Murphy et al., 2016), we can conclude that these analyses are sampling the ground properties in a region of tens of meters around InSight. This is confirmed by the analyses of the miss distances (Section 5.1).

As for the depth in the ground to which we are sensitive: if we were observing the ground deformation from inside the vortex, the depth to which we are sounding would be linked to the size of the vortex. However, in our analyses, we assume that the vortex passes far enough away from the seismometer for the point source

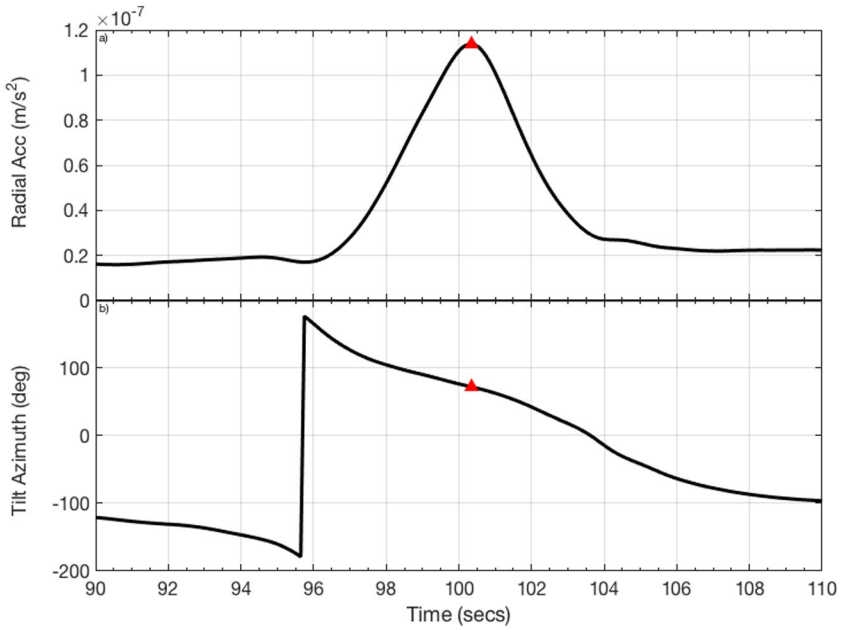

Figure 9. The (a) radial acceleration and (b) azimuth as derived from measurements by SEIS during the vortex event on Sol 133 (April 12, 2019) at 9:51 UTC (12:34 LMST). The red triangle indicates the point of closest approach of the vortex, that is, where the radial acceleration has the largest amplitude. The azimuth of the vortex at the closest approach is 72°.

approximation to be valid ($x > D$). Therefore, the length scale that is important is the distance between the seismometer and the vortex. The ground deformation is then sensitive to depths of a similar length scale, that is, several meters to several tens of meters (Boussinesq, 1885).

5.3. Reconstructing the Convective Vortex Trajectory

Assuming a simple straight line vortex migration, the closest approach of a vortex will be when there is a 90° angle between the vortex trajectory and SEIS. Therefore, calculating the tilt azimuth from the horizontal seismic components at the closest approach provides a first estimate of the vortex trajectory (Figure 9). It is then possible to reconstruct the pressure and seismic time series during the vortex encounter using the point source model described above and in Lorenz et al. (2015). This is a particularly useful tool for verifying the parameter solutions and refining the advection speed and trajectory angle, if necessary.

Figure 10 shows the resulting synthetic seismic acceleration and pressure signal determined for the event shown in Figure 5. The ground and vortex parameter values (η, ζ, x) have been determined using the methodology described in this paper assuming the lower bound on the advection speed ($S = v - 1\sigma_v$). The lower bound of S was used in this example in order to correctly reproduce the vertical seismic signal. The approximate vortex trajectory, as determined by these analyses, is indicated by the yellow arrow in Figure 1.

5.4. Understanding Vortex Trajectories

As mentioned in the previous section, studying the tilt azimuth at the closest approach can give us information on the vortex trajectories. However, when considering the direction of the SEIS tilt at the closest approach (when radial tilt amplitude is largest) it appears that there are very few vortices to the west of InSight and the vast majority of seismic detections of convective vortices have a closest approach to the east of InSight (Figure 11, left). Detailed analyses of orbital satellite (HiRISE) images indicate that there is a preferential orientation for the observed dust devil tracks: in a 12 km^2 area around the lander they are

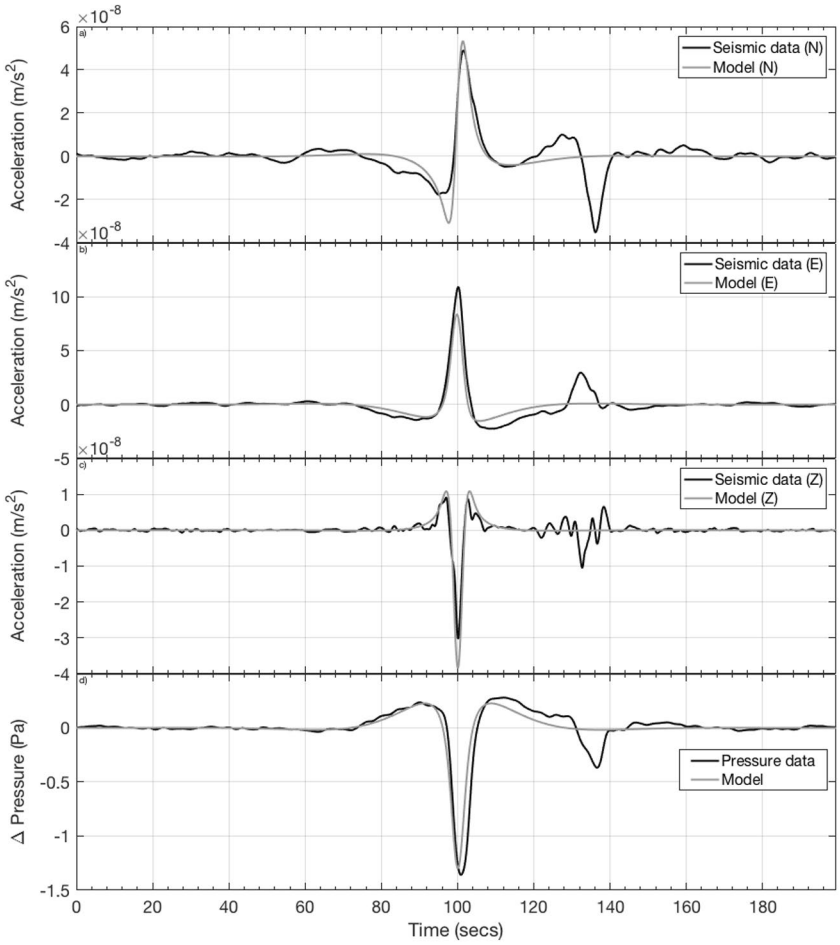

Figure 10. Trajectory reconstruction for the vortex event on Sol 133 (April 12, 2019) at 9:51 UTC (12:34 LMST). The black lines show the seismic and pressure data, the gray lines are the model results. The fit parameters used to reconstruct the seismic and pressure measurements are as follows: $\zeta = 494$ Pa m^2, $\eta = 240$ Pa, $x = 8.2$ m, $S = 3.6$ m/s. These were determined using the methodology presented in this paper. The closest approach azimuth is 72° (Figure 9), and the vortex is assumed to follow a straight line trajectory perpendicular to the closest approach azimuth.

aligned along the mean directions ∼-40° and ∼140° (standard deviation: 24°; Perrin et al., 2020). This is closely aligned with the most common wind direction as measured by TWINS (Perrin et al., 2020; Spiga et al., 2020). However, the dust devil tracks identified in the satellite images are observed to pass on both sides of the InSight lander, theoretically corresponding to the following preferential tilt directions at the vortex closest approaches: ∼55° and ∼-125° (standard deviation: 17°).

This corresponds with the peak in the histogram of vortex detections to the east of InSight, but there is an important discrepancy between the dust devil track observations and the seismic observations to the west of InSight (Figure 11, right).

The possible reasons behind this observed discrepancy have recently been discussed in Golombek et al. (2020). The wind is known to exert lift and drag forces on the lander and the WTS. These aerodynamic forces generate ground deformations at the lander and WTS feet that are then propagated through the ground to the seismometer (Murdoch et al., 2017a, 2018). However, Golombek et al. (2020) suggest that wind drag from the vortex winds is not a plausible explanation for the observed bias as there is no a priori dominant rotation direction of the convective vortices (Kahanpää & Viúdez-Moreiras, 2020; Ringrose et al., 2003; Ryan & Lucich, 1983). In addition, at closest approach, any drag force would not influence the seismic measurement in the tilt direction because the tangential wind velocity is perpendicular to the direction of the tilt. Additionally, the InSight lander is only expected to perturb the vortex trajectories for

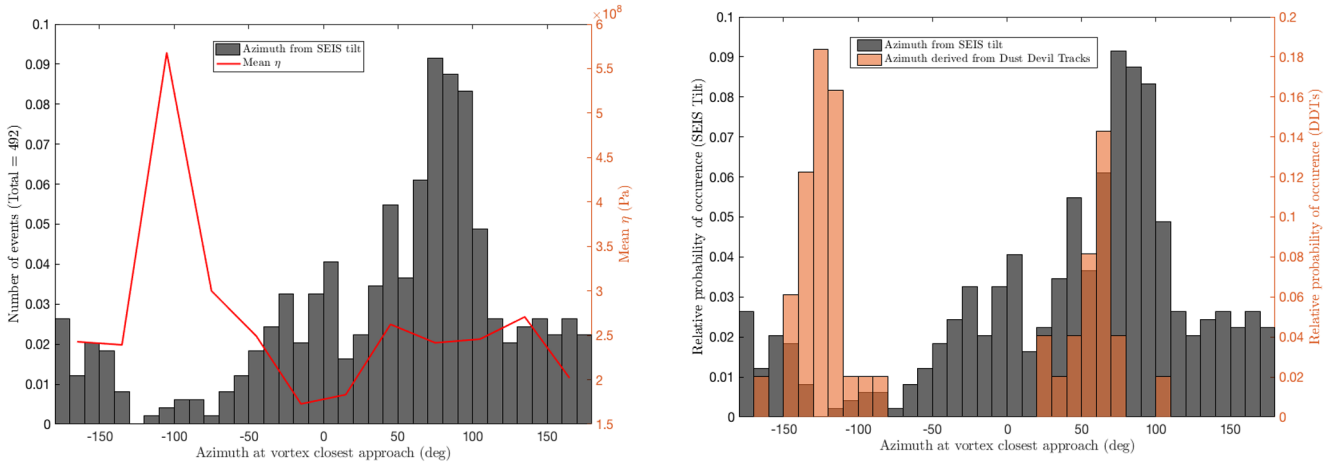

Figure 11. Left: The histogram shows the distribution of the tilt azimuth at the point of closest vortex approach derived from SEIS tilt measurements (when the radial tilt is largest; see example in Figure 9). The SEIS tilt results are for 492 vortex events between sols 75 and 200 (data filtered in the [0.02–0.3 Hz] frequency band). The red line is the mean value of η within bins of 30° of closest approach azimuth in the range of −180 to +180°. Right: Comparison of the distribution of the azimuths at the point of closest approach as measured from the SEIS tilt (black), and derived from dust devil tracks (DDTs) in HiRISE satellite images (orange). The DDTs results shown here are for track detections made in the close vicinity of the lander (49 tracks in an area of about 12 km^2 around the lander; Perrin et al., 2020

direct vortex encounters (i.e., when the center of the vortex passes directly over the lander; Golombek et al., 2020).

The most probable explanation is linked to the ground properties: as a vortex migrates a soft ground will deform more than a hard ground, leading to a larger ground deformation and a larger tilt signal on SEIS. If the ground was softer to the east of InSight compared with the west side, then the number of seismically detected vortices passing to the east would be larger.

Figure 12 shows the distribution of η for all of the vortex events analyzed as a function of the tilt azimuth at their closest approach. These results indicate that the ground is harder to the west; there is a mean η value of ~428 MPa to the west (azimuth −75° to −105°), with respect to ~235 MPa to the east (azimuth 75°–105°). In addition, when compared with the distribution of tilt azimuths (Figure 11, left), the peak in η corresponds to the region where the smallest number of vortices have been detected. Similarly, there are a comparatively larger number of vortex detections to the north than perhaps expected from the dust devil track analyses (Figure 11). This may be due to a softer, more deformable, ground to the north of SEIS.

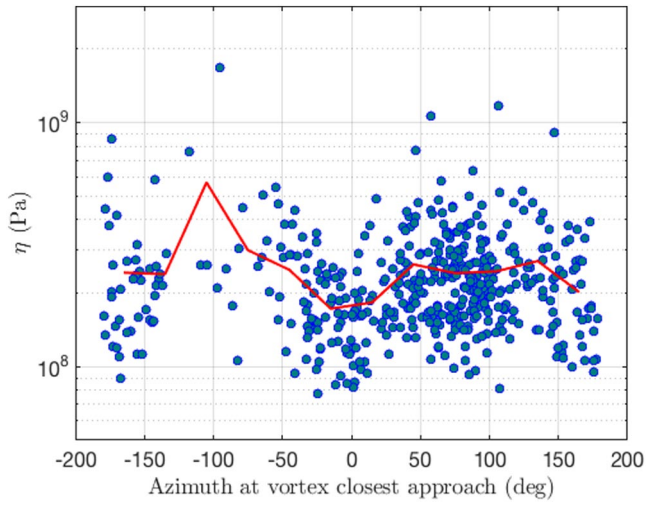

Figure 12. The distribution of η for the 492 vortex events analyzed between sols 75 and 200 as a function of the tilt azimuth at their closest approach. Each circle represents the value η determined for a vortex event. The red line shows the mean value of η binned over 30° of azimuth (corresponds to the red line in Figure 11, left).

These combined results (satellite images, seismic, and pressure observations) imply that there is not a paucity of vortices to the west of InSight but rather a paucity of seismic detections of vortices due to the harder ground to the west.

This observation is consistent with geomorphological and sedimentological surface interpretations of the InSight landing site. InSight landed within a 27-m-diameter, 0.3-m-deep quasicircular depression called Homestead hollow (Figure 1). The hollow is interpreted to be a highly degraded impact crater that has retained its form on the landscape for ~400–700 Myr (Golombek et al., 2020; Sweeney et al., 2018; Warner et al., 2019). Craters near the InSight landing site degrade by a combination of mass wasting, impact gardening, and eolian infilling (Golombek et al., 2020; Sweeney et al., 2018; Warner et al., 2019). Thermal inertia measurements derived from the radiometer onboard InSight and image-based observations from the Instrument Deploy-

ment Camera reveal that the interior of Homestead hollow is dominated by fine sand, with some granules and pebbles. Larger cobble-size clasts, which are common outside of the hollow, are rare in the interior. The hollow is interpreted to be a site of preferential accumulation and preservation of windblown fines. Younger, 10–100-m-scale craters near the landing site exhibit meter-size eolian bedforms against their rims and in their interior. Over time, these bedforms stabilize, plane off, and are replaced by a smooth, dust-mantled surface that is similar to the smooth fill of the hollow. In contrast, the intercrater plains represent a regolith that is also impact gardened and dominated by fine sand, but includes a higher relative abundance of coarser clasts (Golombek et al., 2020). Eolian bedforms, if present on the plains, are out of equilibrium with local wind transport thresholds and eventually migrate to the interiors of impact craters (Grant et al., 2020; Warner et al., 2020). The InSight lander rests along the northwest interior margin of the Homestead hollow, proximal to the contact of these two terrain types (Figure 1, top). Twenty to twenty-five meters of finer hollow fill material stretches to the east and southeast of the lander (Figure 1, bottom). Only 1–5 m of fill separate the lander from the intercrater plains to the west and northwest.

6. Conclusions

Since its landing on Mars the InSight mission has observed multiple convective vortices with both the barometer and seismometers. Here, we present a new computationally inexpensive method that uses the simultaneous pressure and seismic measurements of convective vortices to determine the elastic properties of the Martian subsurface, the vortex properties and their miss distances. Our method also allows the convective vortex trajectories to be reconstructed.

Our results show that η ($\eta = E/[1-\nu^2]$, where E is the Young's modulus and ν is the Poisson's ratio of the Martian ground), in a region of tens of meters around the InSight landing site, is 239 ± 140 MPa (for data filtered in the [0.02–0.3 Hz] frequency band). This is equivalent to a mean Young's modulus of 223 ± 133 MPa assuming a Poisson's ratio of 0.22.

Our analyses are sensitive to ground properties to a depth of several meters to several tens of meters. The elastic properties are consistent with independent subsurface parameter estimations using different methods (Garcia et al., 2020; Kenda et al., 2020; Lognonné et al., 2020).

We also propose that the paucity of seismic detections of vortices to the west of InSight is not due to a smaller number of vortices but rather to the slightly harder, less deformable, ground to the west. This hypothesis is consistent with geomorphological surface interpretations of the InSight landing site; InSight is in a degraded crater ("Homestead Hollow") with a rough/rocky terrain to the west and a smoother terrain with finer material to the east.

One consequence of the variation of the ground elastic properties in the region around SEIS is that the largest seismic tilt signal may not occur at the closest approach, but rather in the region of most deformable ground (lowest Young's modulus). This consideration should be taken into account in future analyses.

We assume that for the pressure drop events included here, the miss distance is larger than the vortex diameter, that is, there are no direct encounters. There are likely to be some close encounters among the events included, however, the majority of the events are not likely to be direct encounters. Therefore, we assume that any errors introduced due to this assumption are likely to be small given the large number of events considered. In the future, such direct encounters could be eliminated from the data set by performing a more detailed study of the wind speed and direction measurements.

Currently, our model trajectories assume a straight-line encounter. However, in the future, more accurate trajectory reconstructions will be performed using the time series of the tilt azimuth. This will also provide an additional method to estimate the miss distance for each vortex encounter.

The new method proposed here to study convective vortices with combined pressure and seismic measurements has the potential to yield both more precise estimates of the elastic properties of the Martian ground, and more extensive statistics of vortex properties and trajectories once further InSight data has been acquired and analyzed.

Data Availability Statement

The raw and calibrated SEIS and APSS data from the InSight mission used in this study are available to the public at the Planetary Data System Geoscience node (InSight Mars SEIS data Service, 2019a), the IPGP Data Center (InSight Mars SEIS data Service, 2019c), and at the IRIS Data Management Center (InSight Mars SEIS data Service, 2019d). A table containing the derived properties of all the vortex events studied in this paper is provided at the following DOI link: 10.5281/zenodo.4436753 (Murdoch, 2021).

Acknowledgments
We acknowledge NASA, CNES, their partner agencies and Institutions (UKSA, SSO, DLR, JPL, IPGP-CNRS, ETHZ, IC, MPS-MPG) and the flight operations team at JPL, SISMOC, MSDS, IRIS-DMC, and PDS for providing SEED SEIS data (InSight Mars SEIS data Service, 2019b). The French authors acknowledge the French Space Agency CNES and ANR (ANR-14-CE36-0012-02 and ANR-19-CE31-0008-08) for support in the Science analysis. R. Lorenz notes the support of NASA via the InSight Participating scientist program grant 80NSSC18K1626. We would also like to thank Jim Murphy and Henrik Kahanpää for their valuable and constructive comments that significantly improved this paper during the review process. This is InSight Contribution Number 108.

References

Balme, M., & Greeley, R. (2006). Dust devils on Earth and Mars. *Reviews of Geophysics*, *44*, RG3003. https://doi.org/10.1029/2005RG000188

Balme, M., Pathare, A., Metzger, S., Towner, M., Lewis, S., Spiga, A., et al. (2012). Field measurements of horizontal forward motion velocities of terrestrial dust devils: Towards a proxy for ambient winds on Mars and Earth. *Icarus*, *221*(2), 632–645. https://doi.org/10.1016/j.icarus.2012.08.021

Banerdt, W. B., Smrekar, S., Banfield, D., Giardini, D., Golombek, M. P., Johnson, C., et al. (2020). Initial results from the InSight mission on Mars. *Nature Geoscience*, *13*, 183–189. https://doi.org/10.1038/s41561-020-0544-y

Banfield, D., Rodriguez-Manfredi, J. A., Russell, C. T., Rowe, K. M., Leneman, D., Lai, H. R., et al. (2019). InSight Auxiliary Payload Sensor Suite (APSS). *Space Science Reviews*, *215*(1), 4. https://doi.org/10.1007/s11214-018-0570-x

Banfield, D., Spiga, A., Newman, C., Forget, F., Lemmon, M., Lorenz, R., et al. (2020). The atmosphere of Mars as observed by InSight. *Nature Geoscience*, *13*(3), 190–198. https://doi.org/10.1038/s41561-020-0534-0

Boussinesq, M. (1885). *Application des potentiels a l'étude de l'équilibre et du mouvement des solides élastiques*. GauthierVillars.

Ellehoj, M. D., Gunnlaugsson, H. P., Taylor, P. A., Kahanpää, H., Bean, K. M., Cantor, B. A., et al. (2010). Convective vortices and dust devils at the Phoenix Mars mission landing site. *Journal of Geophysical Research*, *115*(E14), E00E16. https://doi.org/10.1029/2009JE003413

Ferri, F., Smith, P. H., Lemmon, M., & Rennó, N. O. (2003). Dust devils as observed by Mars pathfinder. *Journal of Geophysical Research*, *108*, 5133. https://doi.org/10.1029/2000JE001421

Garcia, R. F., Kenda, B., Kawamura, T., Spiga, A., Murdoch, N., Lognonné, P. H., et al. (2020). Pressure effects on the SEIS-InSight instrument, improvement of seismic records, and characterization of long period atmospheric waves from ground displacements. *Journal of Geophysical Research: Planets*, *125*(7), e2019JE006278. https://doi.org/10.1029/2019JE006278

Golombek, M. P., Warner, N. H., Grant, J., Hauber, E., Ansan, V., Weitz, C., et al. (2020). Geology of the InSight landing site on Mars. *Nature Communications*, *11*, 1014. https://doi.org/10.1038/s41467-020-14679-1

Grant, J. A., Warner, N. H., Weitz, C. M., Golombek, M. P., Wilson, S. A., Baker, M., et al. (2020). Degradation of homestead hollow at the insight landing site based on the distribution and properties of local deposits. *Journal of Geophysical Research: Planets*, *125*(4), e2019JE006350. https://doi.org/10.1029/2019JE006350

InSight Mars SEIS Data Service. (2019a). *InSight SEIS data Bundle*. PDS Geosciences (GEO) Node. https://doi.org/10.17189/1517570

InSight Mars SEIS Data Service. (2019b). *SEIS raw data, InSight Mission*. IPGP, JPL, CNES, ETHZ, ICL, MPS, ISAE-Supaero, LPG, MSFC. Other/Seismic Network. https://doi.org/10.18715/SEIS.INSIGHT.XB_2016

InSight Mars SEIS Data Service. (2019c). *SEIS raw data, InSight Mission*. IPGP Data Center. Retrieved from http://ws.ipgp.fr/fdsnws/station/1/

InSight Mars SEIS Data Service. (2019d). *SEIS raw data, InSight Mission*. IRIS Data Management Center. Retrieved from http://service.iris.edu/fdsnws/station/1/

Jackson, B., Lorenz, R., & Davis, K. (2018). A framework for relating the structures and recovery statistics in pressure time-series surveys for dust devils. *Icarus*, *299*, 166–174. https://doi.org/10.1016/j.icarus.2017.07.027

Kahanpää, H., Newman, C., Moores, J., Zorzano, M.-P., Martin-Torres, J., Navarro, S., et al. (2016). Convective vortices and dust devils at the MSL landing site: Annual variability. *Journal of Geophysical Research: Planets*, *121*(8), 1514–1549. https://doi.org/10.1002/2016JE005027

Kahanpää, H., & Viúdez-Moreiras, D. (2020). Modelling Martian dust devils using in-situ wind, pressure, and UV radiation measurements by Mars Science Laboratory. *Icarus*. https://doi.org/10.1016/j.icarus.2020.114207

Kenda, B., Drilleau, M., Garcia, R. F., Kawamura, T., Murdoch, N., Compaire, N., et al. (2020). Subsurface structure at the insight landing site from compliance measurements by seismic and meteorological experiments. *Journal of Geophysical Research: Planets*, *125*(6), e2020JE006387. https://doi.org/10.1029/2020JE006387

Kenda, B., Lognonné, P., Spiga, A., Kawamura, T., Kedar, S., Banerdt, W. B., et al. (2017). Modeling of ground deformation and shallow surface waves generated by Martian dust devils and perspectives for near-surface structure inversion. *Space Science Reviews*, *211*(1–4), 501–524. https://doi.org/10.1007/s11214-017-0378-0

Kurgansky, M. (2019). On the statistical distribution of pressure drops in convective vortices: Applications to Martian dust devils. *Icarus*, *317*, 209–214. https://doi.org/10.1016/j.icarus.2018.08.004

Landau, L. D., & Lifshitz, E. M. (1970). *Theory of elasticity, 3rd ed. (volume 7 of a course of theoretical physics)*. Pergamon Press.

Lognonné, P., Banerdt, W. B., Giardini, D., Pike, W. T., Christensen, U., Laudet, P., et al. (2019). SEIS: Insight's seismic experiment for internal structure of Mars. *Space Science Reviews*, *215*(1), 12. https://doi.org/10.1007/s11214-018-0574-6

Lognonné, P., Banerdt, W. B., Pike, W. T., Giardini, D., Christensen, U., Garcia, R. F., et al. (2020). Constraints on the shallow elastic and anelastic structure of Mars from InSight seismic data. *Nature Geoscience*, *13*(3), 213–220. https://doi.org/10.1038/s41561-020-0536-y

Lorenz, R. D., Kedar, S., Murdoch, N., Lognonné, P., Kawamura, T., Mimoun, D., & Bruce Banerdt, W. (2015). Seismometer detection of dust devil vortices by ground tilt. *The Bulletin of the Seismological Society of America*, *105*, 3015–3023. https://doi.org/10.1785/0120150133

Lorenz, R. D., Spiga, A., Lognonne, P., Plasman, M., Newman, C. E., & Charalambous, C. (2021). The whirlwinds of Elysium: A catalog and meteorological characteristics of "dust devil" vortices observed by insight on Mars. *Icarus*, *355*, 114119. https://doi.org/10.1016/j.icarus.2020.114119

Mimoun, D., Murdoch, N., Lognonné, P., Hurst, K., Pike, W. T., Hurley, J., et al. (2017). The noise model of the SEIS seismometer of the InSight mission to Mars. *Space Science Reviews*, *211*(1–4), 383–428. https://doi.org/10.1007/s11214-017-0409-x

Murdoch, N. (2021). *Dataset from "Constraining Martian regolith and vortex parameters from combined seismic and meteorological measurements."* Zenodo. https://doi.org/10.5281/zenodo.4436753

Murdoch, N., Alazard, D., Knapmeyer-Endrun, B., Teanby, N. A., & Myhill, R. (2018). Flexible mode modelling of the InSight Lander and consequences for the SEIS instrument. *Space Science Reviews*, *214*(8), 117. https://doi.org/10.1007/s11214-018-0553-y

Murdoch, N., Mimoun, D., Garcia, R. F., Rapin, W., Kawamura, T., Lognonné, P., et al. (2017a). Evaluating the wind-induced mechanical noise on the InSight seismometers. *Space Science Reviews*, *211*(1–4), 429–455. https://doi.org/10.1007/s11214-016-0311-y

Murdoch, N., Kenda, B., Kawamura, T., Spiga, A., Lognonné, P., Mimoun, D., & Banerdt, W. B. (2017b). Estimations of the seismic pressure noise on Mars determined from large eddy simulations and demonstration of pressure decorrelation techniques for the InSight mission. *Space Science Reviews*, *211*, 457–483. https://doi.org/10.1007/s11214-017-0343-y

Murphy, J., Steakley, K., Balme, M., Deprez, G., Esposito, F., Kahanpää, H., et al. (2016). Field measurements of terrestrial and Martian dust devils. *Space Science Reviews*, *203*(1–4), 39–87. https://doi.org/10.1007/s11214-016-0283-y

Newman, C. E., Kahanpaa, H., Richardson, M. I., Martinez, G. M., Vicente-Retortillo, A., & Lemmon, M. T. (2019). Convective vortex and dust devil predictions for Gale Crater over 3 Mars years and comparison with MSL-REMS observations. *Journal of Geophysical Research: Planets*, *124*(12), 3442–3468. https://doi.org/10.1029/2019JE006082

Perrin, C., Rodriguez, S., Jacob, A., Lucas, A., Spiga, A., Murdoch, N., et al. (2020). Monitoring of dust devil tracks around the InSight Landing Site, Mars, and comparison with in situ atmospheric data. *Geophysical Research Letters*, *47*(10), e87234. https://doi.org/10.1029/2020GL087234

Rafkin, S., Jemmett-Smith, B., Fenton, L., Lorenz, R., Takemi, T., Ito, J., & Tyler, D. (2016). Dust devil formation. *Space Science Reviews*, *203*(1–4), 183–207. https://doi.org/10.1007/s11214-016-0307-7

Reiss, D., Spiga, A., & Erkeling, G. (2014). The horizontal motion of dust devils on Mars derived from CRISM and CTX/HiRISE observations. *Icarus*, *227*, 8–20. https://doi.org/10.1016/j.icarus.2013.08.028

Ringrose, T., Towner, M., & Zarnecki, J. (2003). Convective vortices on Mars: A reanalysis of Viking Lander 2 meteorological data, sols 1-60. *Icarus*, *163*(1), 78–87. https://doi.org/10.1016/S0019-1035(03)00073-3

Ryan, J. A., & Lucich, R. D. (1983). Possible dust devils, vortices on Mars. *Journal of Geophysical Research*, *88*(C15), 11005–11011. https://doi.org/10.1029/JC088iC15p11005

Scholz, J.-R., Widmer-Schnidrig, R., Davis, P., Lognonné, P., Pinot, B., Garcia, R. F., et al. (2020). Detection, analysis and removal of glitches from InSight's seismic data from Mars. *Earth and Space Science Open Archive*, *7*, e2020EA001317. https://doi.org/10.1002/essoar.10503314.2

Sorrells, G. G. (1971). A preliminary investigation into the relationship between long-period seismic noise and local fluctuations in the atmospheric pressure field. *Geophysical Journal International*, *26*, 71–82. https://doi.org/10.1111/j.1365-246X.1971.tb03383.x

Sorrells, G. G., McDonald, J. A., & Herrin, E. T. (1971). Ground motions associated with acoustic waves. *Nature Physical Science*, *229*, 14–16. https://doi.org/10.1038/physci229014a0

Spiga, A., Banfield, D., Teanby, N. A., Forget, F., Lucas, A., Kenda, B., et al. (2018). Atmospheric science with InSight. *Space Science Reviews*, *214*(7), 109. https://doi.org/10.1007/s11214-018-0543-0

Spiga, A., Murdoch, N., Lorenz, R., Forget, F., Newman, C., Pla-Garcia, J., et al. (2020). A study of daytime convective vortices and turbulence in the Martian Planetary Boundary Layer based on half-a-year of InSight atmospheric measurements and Large-Eddy simulations. *Journal of Geophysical Research: Planets*, *126*, e2020JE006511. https://doi.org/10.1029/2020JE006511

Stanzel, C., Pätzold, M., Williams, D. A., Whelley, P. L., Greeley, R., Neukum, G., et al. (2008). Dust devil speeds, directions of motion and general characteristics observed by the mars express high resolution stereo camera. *Icarus*, *197*(1), 39–51. https://doi.org/10.1016/j.icarus.2008.04.017

Steakley, K., & Murphy, J. (2016). A year of convective vortex activity at gale crater. *Icarus*, *278*, 180–193. https://doi.org/10.1016/j.icarus.2016.06.010

Sweeney, J., Warner, N. H., Ganti, V., Golombek, M. P., Lamb, M. P., Fergason, R., & Kirk, R. (2018). Degradation of 100-m-scale rocky ejecta craters at the InSight Landing site on Mars and implications for surface processes and erosion rates in the Hesperian and Amazonian. *Journal of Geophysical Research: Planets*, *123*(10), 2732–2759. https://doi.org/10.1029/2018JE005618

Tratt, D. M., Hecht, M. H., Catling, D. C., Samulon, E. C., & Smith, P. H. (2003). In situ measurement of dust devil dynamics: Toward a strategy for Mars. *Journal of Geophysical Research*, *108*, E11. https://doi.org/10.1029/2003JE002161

Vatistas, G. H., Kozel, V., & Mih, W. C. (1991). A simpler model for concentrated vortices. *Experiments in Fluids*, *11*(1), 73–76. https://doi.org/10.1007/BF00198434

Warner, N. H., Golombek, M. P., Grant, J., Wilson, S., Hauber, E., Ansan, V., et al. (2019). *Geomorphology and origin of Homestead hollow, the landing location of the InSight Lander on Mars*. Lunar and Planetary Science Conference, p. 1184.

Warner, N. H., Grant, J., Wilson, S., Golombek, M., DeMott, A., Charalambous, C., et al. (2020). An impact crater origin for the InSight landing site at Homestead Hollow, Mars: Implications for near surface stratigraphy, surface processes, and erosion rates. *Journal of Geophysical Research: Planets*, *125*(4), e2019JE006333. https://doi.org/10.1029/2019JE006333